Journal of Ceramic Processing Research. Vol. 24, No. 2, pp. 329~335 (2023)
(Received 11 October 2022, Received in revised form 16 December 2022, Accepted 31 December 2022)
https://doi.org/10.36410/jcpr.2023.24.2.329

J O U R N A L O F
Ceramic Processing Research

The influence mechanism of modified calcium bentonite on drying shrinkage of alkali-activated material

Li Wanqiang[a,b], Jiang Chunmeng[a,b,*] and Li Shuangxi[a,b]
[a]*College of Water Conservancy and Civil Engineering, Xinjiang Agricultural University, Urumqi 830052, PR China*
[b]*Xinjiang Key Laboratory of Hydraulic Engineering Security and Water Disasters Prevention, Urumqi 830052, PR China*

Volumetric instability is one of the main reasons restricting the engineering application of alkali-activated material (AAM). The aim of this work is to determine the most convenient calcination temperature of calcium bentonite (CB) to reduce the drying shrinkage of AAM. Five temperature gradients (20 °C, 150 °C, 600 °C, 750 °C, 900 °C) and three admixture levels (5%, 10%, 15%) were considered. The results show that a calcination temperature of 150 °C and 15% admixture is the optimum treatment. The compressive strength of the AAM is improved, and the drying shrinkage is substantially reduced. The x-ray diffraction, scanning electron microscope, and mercury intrusion porosimetry tests have shown that calcination at 150 °C enhanced the interlayer properties for better performance than AAM prepared by dehydroxylation of CB calcined at high temperatures. The water retention reduces the evaporation of water and generates N-A-S-H gels after dissolution. Causes coarsening of the pore size of the AAM and reduced drying shrinkage.

Keywords: Alkali-activated, Calcium bentonite, Drying shrinkage, Pore structure.

Introduction

Cement is one of the most basic building materials in the world. However, the production of cement is accompanied by significant energy consumption and greenhouse gas emissions. Each tonne of cement manufactured emits approximately 1 ton of CO_2, accounting for roughly 5-7% of all human-generated carbon emissions [1, 2]. With the growing demand for sustainable building materials, alkali-activated material (AAM) are becoming the focus in the construction sector.

The main raw materials for AAM are industrial by-products or waste, such as slag [3], fly ash [4], and metakaolin [5]. Therefore, the production process consumes fewer resources and energy, and the carbon emissions are reduced by about 80% of the ordinary Portland cement (OPC) [6, 7]. The alkali-activated reactivity is derived from the decomposition and recombination of the active substances in an alkaline environment. The main hydration products of AAM can be classified as C-A-S-H gels and N-A-S-H gels [8, 9], which depend on the percentage of the calcium content of the raw material. The dense gels network offers AAM many advantages, such as early strength [10], fire resistance [11], and corrosion resistance [12]. However, the dense structure increases the number of mesopores and reduces volume stability, resulting in the drying shrinkage of AAM being 3-4 times higher than that of OPC [13].

Optimizing the mix ratio is considered an effective way of reducing the drying shrinkage of AAM. The combination of different materials allows the conversion from N-A-S-H to C-A-S-H gels or coexistence [14]. It indicates that the performance of AAM can be controlled by blending the proportions of the materials. Among the various raw materials for AAM, metakaolin is considered to be of significant potential [15]. The kaolinite used to make metakaolin is classified as a 1:1 layered structure type of clay consisting of a layer of alumina-oxygen tetrahedra connected to a layer of silica-oxygen tetrahedra [16, 17]. The metakaolin not only enhances the strength of AAM but also performs better in durability [18]. Unfortunately, there is not much distribution of kaolinite-rich minerals, and metakaolin is widely demanded by other industries [19].

Bentonite is a 2:1 type of clay consisting of two layers of silica-oxygen tetrahedra and one layer of aluminum-oxygen octahedra, and the main component is montmorillonite [16]. Montmorillonite has large and variable interlayer spacing, which allows the exchange of cations or storage of water molecules [20, 21]. Bentonite is not fully applicable as a cementitious material component due to its weak pozzolanic activity [22]. But bentonite can also be made more reactive by calcining to remove the hydroxyl group, as is the case with metakaolin [23]. In recent years, bentonite has

*Corresponding author:
Tel : +86-13209901058
E-mail: jiangcm93@163.com

begun trying to mix into the AAM. The interlayer structure of bentonite can exchange excess cations, and the dissolved bentonite can be used as a template for gels precipitation and participate in hydration reactions [24, 25].

This study aimed to evaluate the role that CB plays in resisting the drying shrinkage of AAM. CB calcined at low-temperature and high-temperature conditions, combined with different admixture levels, and the results of the study may be useful to expand the range of bentonite applications.

Experimental

Materials

The chemical components of slag, fly ash, cement, and CB were determined using X-ray fluorescence (XRF, ARL PERFORM'X model), and the results are listed in Table 1. The slag grade is S75, the fly ash is low-calcium ClassII F, provided by the Yuance Co. (Changji, China). The CB was a low-purity untreated raw mineral, provided by Xiangshui Building Materials Co. (Yueyang, China). Water glass and flake sodium hydroxide are provided by Jinxin Factory (Urumqi, China). The SiO_2/Na_2O of the water glass is 3.0, and the flaky sodium hydroxide purity is >99%.

Before sample preparation, mix the flake sodium hydroxide with sodium silicate in a certain ratio and fix the modulus to 1.4 and cool to room temperature for use. The CB was sieved and calcined in a horse boiling furnace at 150 °C, 600 °C, 750 °C, and 900 °C for 2 h.

Compressive strength

The compressive strength specimens were prepared according to the Chinese standard (GB/T 17671-1999 Method of testing cements-Determination of strength ISO method) with 40×40×160 mm. The total weight of the cementitious material was 450 g. The specimens

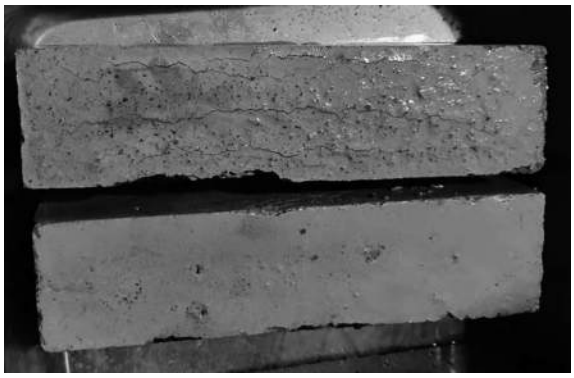

Fig. 1. Cracking in AAM mortar admixture of 20% CB.

Table 1. Chemical composition of the main mineral materials (wt.%).

Raw materials	CaO	SiO_2	Al_2O_3	SO_3	MgO	Fe_2O_3	TiO_2	K_2O	LOI
Slag	39.3	34.53	12.73	0.4	8.27	1.93	0.9	0.8	0.3
Fly ash	4.8	56.2	22.5	1.02	1.56	5.09	1.8	0.9	3.8
CB	1.62	71.2	13	-	2.71	0.75	0.1	1.01	7.35

Table 2. Detailed composition of AAM.

Mixtures	Slag (wt%)	Fly ash (wt%)	CB (wt%)	Calcination temperature (°C)	Na_2SiO_3 (Na_2O wt%)	w/b
Control	80	20	0	-	5	0.5
AAM-1	75	20	5	20	5	0.5
AAM-2	70	20	10	20	5	0.5
AAM-3	65	20	15	20	5	0.5
AAM-4	75	20	5	150	5	0.5
AAM-5	70	20	10	150	5	0.5
AAM-6	65	20	15	150	5	0.5
AAM-7	75	20	5	600	5	0.5
AAM-8	70	20	10	600	5	0.5
AAM-9	65	20	15	600	5	0.5
AAM-10	75	20	5	750	5	0.5
AAM-11	70	20	10	750	5	0.5
AAM-12	65	20	15	750	5	0.5
AAM-13	75	20	5	900	5	0.5
AAM-14	70	20	10	900	5	0.5
AAM-15	65	20	15	900	5	0.5

were placed in the maintenance condition of ±20 ℃ and more than 95% relative humidity, covered with cling film. The compressive strength test was carried out after maintenance to the specified age, and the results were taken as the average of the three groups.

Drying shrinkage

Preparation of AAM drying shrinkage samples according to Chinese standards (JCT603-2004 Standard test method for drying shrinkage of mortar), the proportion of cementitious material is consistent with the compressive strength. The two ends of the mold are pre-buried with copper nail heads, and the size is 25×25×280 mm. After pouring and forming, the mold was placed in a cement mortar curing box with a temperature of (20±2) °C and humidity of (90±5)% for 24 h. Remove the mold and test its initial length L_0 with a length ratio meter. Then put the specimen in a drying shrinkage curing box with a temperature of (20±3) °C and humidity of (50±4)% for curing. When the specimen is cured to a specified age t, the length L_t of the specimen is tested. The drying shrinkage of the AAM S_t specimen is calculated according to Eq (1), and the test result is taken as the average value of three specimens.

$$S_t = \frac{(L_0 - L_t) \times 100}{250} \quad (1)$$

Micro evaluation for the AAM

The X-ray diffraction (XRD, X'PertPRO model) test was used to observe the crystalline phase of the sample. The instrument used CuKα radiation, a scanning speed of 2°/min, a voltage of 40 kV, and a scanning range of 10-80°. CB passed 200 mesh sieve before a test. AAM samples were selected from the compressive strength test after crushing the central area of the test block, the use of anhydrous ethanol to terminate hydration, an electric blast dryer 50 ℃ to constant weight after grinding, and passing 200 mesh sieve after using powder observation.

The Scanning electron microscope (SEM) test used the instrument model ZEISS2, voltage 20 kV. Before the test, the surface was dried and sprayed with gold to enhance electrical conductivity.

The Mercury intrusion porosimetry (MIP) test was performed by AutoPore IV 9500 with a maximum pressure of 33,000 pounds and a pore size test range of 5 nm-1000 um.

Results and Discussion

Crystal Phase Change of CB

Fig. 2 shows the XRD diffraction patterns of CB calcined at different temperatures. The main component of the CB is montmorillonite, and the impurities are muscovite, albite, and quartz. There was no significant

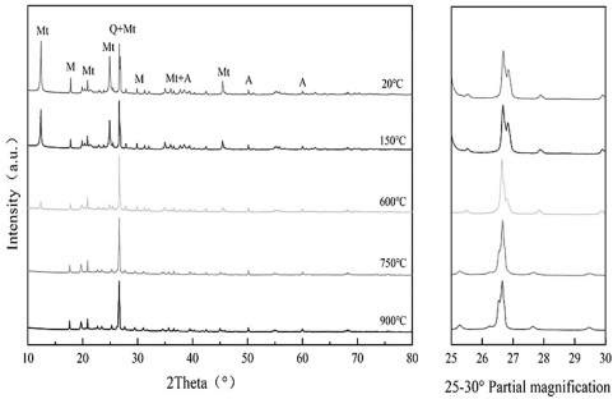

Fig. 2. XRD pattern of CB (Mt-montmorillonite, M-muscovite, Q-quartz, A-albite).

change in the crystalline phase between 20 °C and 150 °C. A decrease in the area of the montmorillonite diffraction peak was calculated by Jade, which may be related to the loss of interlayer water [26]. The low-temperature calcination did not change the properties of CB, but the loss of interlayer water enhanced the water absorption and ion exchange ability. After calcination at 600 °C, the intensity of the diffraction peak of montmorillonite decreased significantly, the structure of montmorillonite started to collapse, an incomplete dehydroxylation reaction occurred, and the structure of montmorillonite was partially retained and partially transformed into amorphous aluminosilicate. At 750 °C, the diffraction peak of montmorillonite disappeared utterly, and the structure fully decomposed into an amorphous phase [27, 28]. At 900 °C, the diffraction peak of montmorillonite disappeared, while the pattern of 26.7° quartz reversed, and the diffraction intensity increased. This may be attributed to the recrystallization reaction, a new crystalline phase was generated.

Mechanical properties of the AAM

Fig. 3 shows the effect of the calcined CB content on the compressive strength of the AAM within 28d. It can be seen that the effect of CB on the compressive resistance of AAM is multifaceted, and shows a complex fluctuating trend with the changes in calcination temperature. According to the XRD test results, CB is completely dehydroxylated at 750 °C and has the highest reactivity. However, this is not consistent with the compressive strength, which does not exceed that of the control group at 750 °C. Interestingly, the optimum treatment temperature is 150 °C, which has the highest strength.

Similarly, the relationship between strength and admixture is not a linear increase or decrease. The property status of the CB can explain the variability of these results. Under the conditions of low-temperature calcination, removing the hydroxyl groups from the

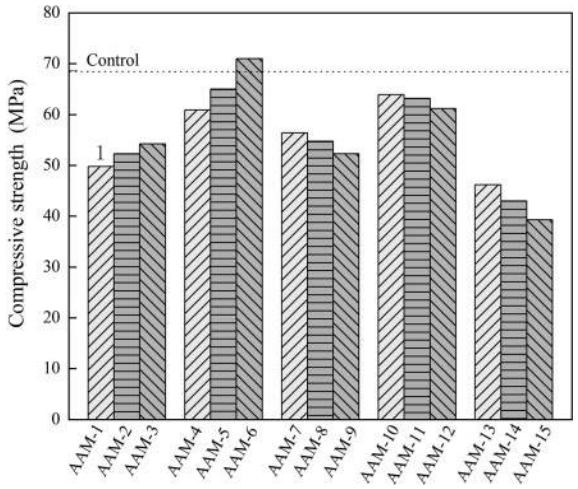

Fig. 3. 28 days compressive strength of the AAM.

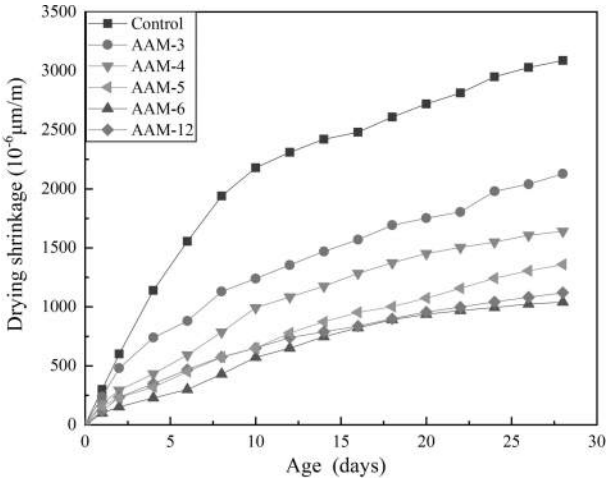

Fig. 4. 28 days drying shrinkage of the AAM.

bentonite is insufficient, and the interlayer properties are retained. 150 °C allows the bentonite to remove the interlayer moisture to obtain enhanced adsorption properties. The interlayer ion exchange properties of bentonite have been shown to adsorb Na^+ and reduce the hindering effect of excess alkaline metal cations on hydration reactions [25]. Under high-temperature calcination conditions, the CB undergoes a dehydroxylation reaction, resulting in the inter-polyhedral links being broken, the collapse of the 2:1 structure and the loss of all interlayer properties. Combined with the changes in the crystalline phase, 600 °C was in a semi-stable state, with part of the montmorillonite dehydroxylated and part of the montmorillonite retaining crystalline properties. At 750 °C, the CB is in an amorphous state and undergoes a complete dehydroxylation reaction with the highest reactivity. The recrystallization reaction takes place at 900 °C. The amorphous phase is transformed into an ordered crystalline phase, and the reactivity decreases.

Drying shrinkage behavior of the AAM

Fig. 4 shows the drying shrinkage behavior of the AAM. It can be seen that the drying shrinkage of AAM with a maximum value of 3088 mm/m at 28 d. Generally, the shrinkage of the AAM can be divided into two stages [29]. The first stage ends at around 7 days with a rapid growth rate of drying shrinkage, which caused by the evaporation of water due to the humidity gradient. The second stage of drying shrinkage growth rate slows down after 7 days, and it is mainly attributed to hydration reactions.

The drying shrinkage of the AAM was reduced by the admixture of CB, with improvements in both the first and second stages. The improvement is related to the amount of admixture and the calcination temperature. The first low value occurred at low-temperature calcination of 150 °C. As the modification temperature increased, the drying shrinkage increased and then decreased. A second low value occurred at 750 °C. It is hypothesized that the drying shrinkage behavior of AAM is closely related to the water absorption capacity and the amount of dehydroxylation of bentonite. The first stage is usually the period of accelerated shrinkage, when the free water content is highest. 150 °C calcined bentonite can adsorb large amounts of free water, generating a smaller first stage of drying shrinkage. The bentonite calcined at 750 °C lost its water absorption, the first stage drying shrinkage grows relatively fast, but has a relatively small second stage drying shrinkage.

Pore Characteristics of the AAM

There are four classes according to the pore size, below 4.5 nm is gel micropores of harmless pores, 4.5-50 nm is the mesopores level of harmful pores, 50-100 nm is the middle capillary pores of multi-harmful pores, and above 100 nm is the large capillary pores [30]. According to the Washburn equation, the smaller the pore size, the higher the meniscus pressure [31].

Table 3. The pore characteristics of the AAM.

Specimen	Porosity (vol%)	Median diameter (nm)	Average pore diameter (nm)
Control	10.81	5.96	7.36
AAM-3	20.23	13.29	12.78
AAM-6	14.94	7.81	8.27
AAM-12	15.64	8.94	8.63

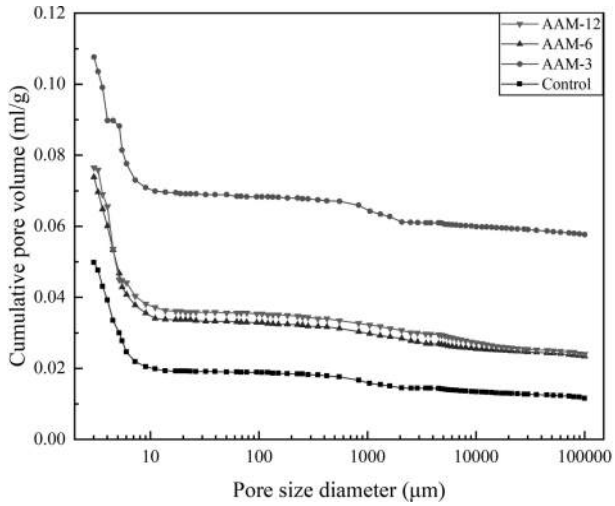

Fig. 5. The pore volume of the AAM.

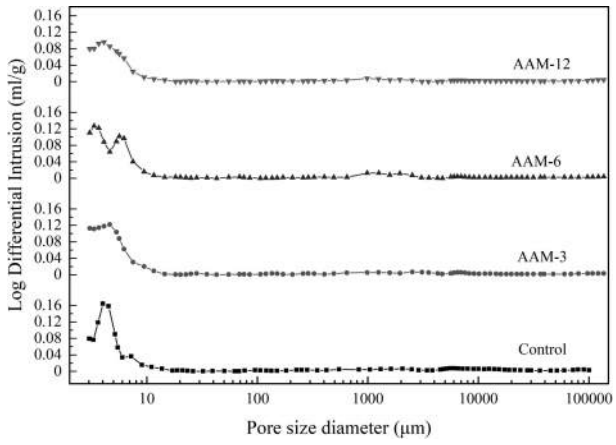

Fig. 6. The pore size distribution of the AAM.

The AAM matrix becomes denser and reduces volume under the shrinkage stress [32].

$$d = -\frac{4\gamma\cos\theta}{P} \quad (2)$$

Where γ is the surface tension of mercury, θ is the contact angle between mercury and pore wall, d is the pore diameter, and P is the capillary pressure Eq. (2).

The porosity and pore size distributions of the AAM are shown in Fig. 5 and Fig. 6. The pore structure affects the form of water presence and transport in cementitious materials, which further determines the drying shrinkage behavior. The control group had the smallest total porosity of 10.81% and the median pore size of 5.96 nm (Table 2), followed by AAM-6 and AAM-12, and the largest porosity was AAM-3. The incorporation of CB increased the porosity of AAM, and the pore size of the mesopores increased. 150 °C and 750 °C had not significantly differ in porosity and pore size, but the values were higher than the control group.

The pattern of pore size changes can be derived by combining with the crystalline phase changes in CB during heat treatment and macroscopic test results. The rate of water absorption of CB is higher than the hydration reaction. The absorbed water has a moisturizing effect on the CB, increasing the internal relative humidity of the AAM and slowing down the rate of water release. As a result, the first stage of AAM drying shrinkage is low. In the second stage, CB retains an intact structure in the early stages of hydration. The CB is dissolved by the erosion of the alkali component and participates in the hydration reaction as a template for the gels precipitation. CB dissolution leaves pores, and dissolution-precipitation does not return to a filled state, resulting in high porosity and reduced drying shrinkage.

Hydration Micromorphology of the AAM

Uncalcined bentonite is layered, with large interlayer spacing to store water or exchange ions (Fig. 7-a). Fig.

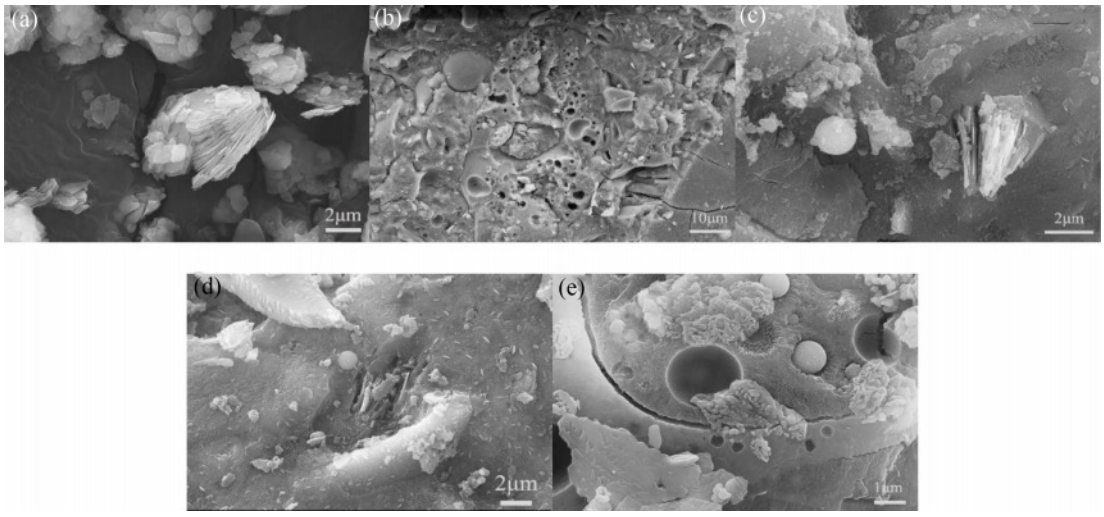

Fig. 7. Hydration micromorphology of the AAM.

7-b shows typical dense and continuous N-A-S-H gels surrounded by spherical particles of incompletely hydrated fly ash and a concentrated distribution of pores of varying sizes [33]. The hydration reaction in the control group was inadequate, and the rapid rate of reaction prevented effective contact between the reactants. CB particles can be seen embedded in the structure accompanied by unhydrated fly ash in the AAM-3 (Fig. 7-c). The dissolved flake CB builds up, and the N-A-S-H gels grow on the precipitated template and separate from the unhydrated fly ash. The fly ash and dissolved CB within the AAM-6 (Fig. 7-d) sample are highly hydrated and tightly bonded to the matrix. In contrast, AAM-12 (Fig. 7-e) has a high degree of hydration reaction and no embedded layered CB particles. There are some holes left by the hydration of fly ash, attached with collapsed plate-like structures and semi-hydrated fly ash particles.

The crystal phase of hydration products of the AAM

The XRD results of AAM curing for 28 days are shown in Fig. 8. The main crystalline phases in AAM are hydrous calcium zeolite and quartz. Hydrated zeolites are highly crystalline gels derived from the polymerization of aluminous siliceous materials by hydration reactions. The quartz comes from partially grinded standard sand. The uncrystallized N-A-S-H gels can be observed from the diffusion peak packet near the 27.3°-30° diffraction angle, and the diffraction peak is relatively insignificant. In addition, hydrotalcite and mullite are displayed in the physical phase. Hydrotalcite may come from C-A-S-H gels, and mullite is a component contained in fly ash [34, 35].

There was no obvious formation or disappearance of new crystalline phases in the physical phase of AAM samples. The differences among the samples were shown in the intensity values of the diffraction peaks. Moreover, the diffraction peaks of montmorillonite were not found in any of the AAM samples, and this may be related to the dissolution-precipitation effect of montmorillonite, which acted as a reactant to produce hydrated gels. The diffraction peaks of hydrated calcium zeolite decreased with the increase of CB modification temperature, and the composition of mullite was slightly enhanced, which may be related to the difference in the hydration process.

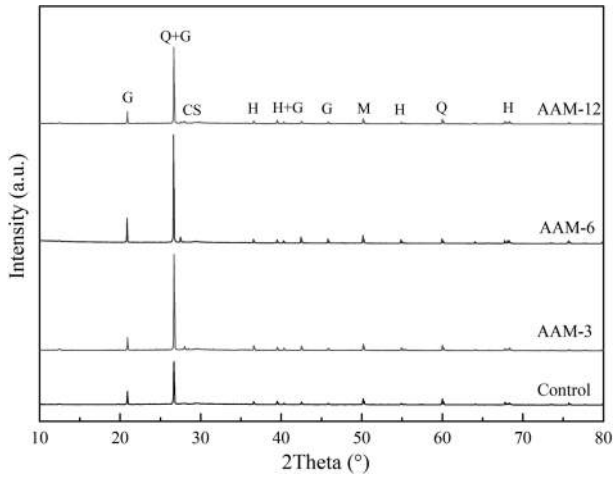

Fig. 8. The crystal phase composition of the AAM (G-gismondine,Q-quarz, CS-C-S-H gel, H-herchelite, M-mullite).

Conclusions

In this study, the effect of drying shrinkage properties of CB in AAM at different calcined temperatures and admixture levels was investigated. Based on the results of the tests, the following conclusions can be drawn.

(1) The reactivity of CB is very weak and has a negative effect on the compressive strength of AAM. CB can be modified by calcination to increase reactivity. The increase in strength is closely related to the interlayer properties of CB, with ionic exchangeability and dehydroxylation reactions compatible with AAM. 150 °C and 750 °C calcination can achieve the strength requirements of AAM.

(2) The admixture of CB has a positive effect on the drying shrinkage of AAM. Calcination improves the shrinkage reduction capacity of the CB, and 150 °C is the appropriate temperature for calcination. The results of the MIP tests indicate that low porosity and high mesopores distribution are responsible for the high drying shrinkage of AAM. CB reduces drying shrinkage by coarsening the pores and increasing the size of the mesopores.

(3) The difference in shrinkage of calcined CB comes from the interlayer properties. The mechanism of shrinkage in low-temperature calcined CB is attributed to moisture retention due to water absorption, which slows down the rate of water evaporation.

Acknowledgments

This research was funded by the Open Fund Project of Xinjiang Key Laboratory of Hydraulic Engineering Security and Water Disasters Prevention (ZDSYS-JS-2022-09); 2022 Xinjiang Agricultural University High Level Talent Research Cultivation Program (2522GCCRC); Xinjiang Key Laboratory of Hydraulic Engineering Security and Water Disasters Prevention (ZDSYS-YJS-2022-21); the Natural Science Foundation of Xinjiang Uygur Autonomous Region (2019D01A46). The authors would like to thank Wang Minglong from Shiyanjia Lab (www.shiyanjia.com) for the XRD analysis.

Conflicts of interest: The authors declare that they have no known competing financial interests or personal relationships that could have appeared to influence the work reported in this paper.

References

1. Y. Kim and T. Chae, J. Ceram. Process. Res. 19[5] (2018) 378-382.
2. M. Mastali, P. Kinnunen, A. Dalvand, R.M. Firouz, and M. Illikainen, Constr. Build. Mater. 190 (2018) 533-550.
3. X. Hu, C.J. Shi, Z.H. Zhang, and Z.L. Hu, J. Am. Ceram. Soc. 102[8] (20119) 4963-4975.
4. Q.B. Tian, D.Q. Sun, Z.Y. Gua, and Z.J. Lv, J. Ceram. Process. Res. 21[3] (2020) 358-364.
5. Y. Rho and S.G. Kang, J. Ceram. Process. Res. 21 (2020) S74-S80.
6. P. Duxson, J.L. Provis, G.C. Lukey, and J. Deventer, Cem. Concr. Res. 37[12] (2007) 1590-1597.
7. Y. Kim, S. Kim, and C. Jang, J. Ceram. Process. Res. 17[11] (2016) 1202-1207.
8. I. Garcia-Lodeiro, A. Fernandez-Jimenez, A. Palomo, and D.E. Macphee, J. Am. Ceram. Soc. 93[7] (2010) 1934-1940.
9. J. Yang, D. Li, and Y. Fang, Constr. Build. Mater. 167(2018) 65-72.
10. S.H. Jeon, S.M. Kang, M.S. Song, and K.N. Kim, J. Ceram. Process. Res. 19[4] (2018) 332-336.
11. S.K. Nath, S. Mukherjee, S. Maitra, and S. Kumar, Trans. Indian. Ceram. Soc. 73[2] (2014) 126-132.
12. T.A. Aiken, J. Kwasny, W. Sha, and K.T. Tong, Constr. Build. Mater. 301 (2021) 124330.
13. M. Chi, Constr. Build. Mater. 35 (2012) 240-245.
14. T. Yang, X. Yao, and Z. Zhang, J. Sustain. Cem-Based. 1[4] (2012) 167-178.
15. T. Bai, Z.-G. Song, Y.-G. Wu, X.-D. Hu, and H. Bai, Ceram. Int. 44[13] (2018) 15706-15713.
16. S.C. Taylor-Lange, E.L. Lamon, K.A. Riding, and M.C.G. Juenger, Appl. Clay. Sci. 108 (2015) 84-93.
17. S. Demir and S. Yasin, J. Ceram. Process. Res. 23[1] (2022) 41-47.
18. L. Li, Z.H. Xu, H. Li, J.Y. Li, D. Hu, Y.L. Xiang, L.P. Han, and X. Peng, Ceram. Int. 48[11] (2022) 15236-15242.
19. H.H. Murray, Appl. Clay. Sci. 17[5-6] (2000) 207-221.
20. M.H. Morcali, J. Ceram. Process. Res. 17[2] (2016) 85-90.
21. Z. Sun, Y.-g. Chen, Y.-j. Cui, H.-d. Xu, W.-m. Ye, and D.-b. Wu, Eng. Geol. 244 (2018) 66-74.
22. J. Ahmad, K.J. Kontoleon, M.Z. Al-Mulali, S. Shaik, M.H. El Ouni, and M.A. El-Shorbagy, Buildings. 12[5] (2022) 634.
23. L. Valentini, S. Contessi, M.C. Dalconi, F. Zorzi, and E. Garbin, J. Cleaner Prod. 184 (2018) 41-49.
24. W.P. Gates and A. Bouazza, Geotext. Geomembr. 28[2] (2010) 219-225.
25. Y. Huang, Trans. Indian. Ceram. Soc. 79[2] (2020) 77-82.
26. R. Fernandez, F. Martirena, and K.L. Scrivener, Cem. Concr. Res. 41[1] (2011) 113-122.
27. Y. El Ouardi, C. Branger, K. Laatikainen, G. Durrieu, S. Mounier, A. Ouammou, and V. Lenoble, Sep. Sci. Technol. 56[15] (2021) 2521-2531.
28. Y.T. Qin, T.J. Peng, H.J. Sun, L. Zeng, Y. Li, and C. Zhou, Clays. Clay. Miner. 69[3] (2021) 328-338.
29. A.M.N. Antonio, A.C. Maria, and Wellington, Cem. Concr. Res. 38 (2008) 565-574.
30. Q. Zeng, K.F. Li, T. Fen-Chong, and P. Dangla, Cem. Concr. Res. 42[1] (2012) 194-204.
31. Y. Ma, J. Hu, and G. Ye, Fuel. 104 (2013) 771-780.
32. M. Palacios and F. Puertas, Cem. Concr. Res. 37[5] (2007) 691-702.
33. I. Garcia-Lodeiro, A. Palomo, A. Fernandez-Jimenez, and D.E. Macphee, Cem. Concr. Res. 41[9] (2011) 923-931.
34. M.S.H. Khan, O. Kayali, and U. Troitzsch, Cem. Concr. Compos. 81 (2017) 49-58.
35. S. Wattanasiriwech, F.A. Nurgesang, D. Wattanasiriwech, and P. Timakul, Ceram. Int. 43[18] (2017) 16063-16069.